Journal of Power, Energy, and Control

Research article

Observer-Assisted Compensation of Three-Phase Current Unbalance in Scott-Transformer Railway Power Systems Using Back-to-Back Converters

Benjamin Egyin Wilson[1]*, Bernard Arhin[2], Md Nur-A-Adam Dony[3], Emmanuel Agyepong Nyantakyi[1]

[1]Department of Electrical Engineering, University of Energy and Natural Resources, Sunyani, Ghana
[2]Department of Electrical Engineering, Chungnam National University, Daejeon, Republic of Korea
[3]Department of Electrical Engineering, Pennsylvania State University, University Park, PA, United States
*Correspondence: benjamin.wilson@uenr.edu.gh

https://doi.org/10.62777/pec.v3i2.117

Received: 16 March 2026
Revised: 24 May 2026
Accepted: 20 June 2026
Published: 22 September 2026

Abstract: This paper presents an experimental comparison of two control strategies for mitigating three-phase current unbalance in Scott-transformer-fed railway power systems. Both methods employ the same single-phase three-level back-to-back converter, but they differ in the variable used to generate the compensation command. The first strategy derives the reference from load-side active and reactive power, whereas the second generates the reference directly from the Scott-transformer secondary current, thereby targeting the source-side balance condition more directly. To ensure reliable synchronization under low-switching-frequency operation and notch-distorted secondary voltage, an observer-assisted synchronous reference frame phase-locked loop is adopted ahead of the control stage. The proposed approaches are validated experimentally on a 5 kVA laboratory prototype. The measured results show that the three-phase current-unbalance ratio is reduced from 34.2% before compensation to 2.8% with the power-based strategy and to 1.2% with the current-based strategy. In addition, both methods maintain stable DC-link operation and exhibit comparable harmonic and current-tracking performance. These results demonstrate that source-current-oriented compensation based on Scott-transformer secondary current provides superior balancing performance for railway applications with strongly varying single-phase loads.

Keywords: Scott transformer, railway power system, three-phase current unbalance, back-to-back converter, current-based compensation, observer-assisted synchronization.

1. Introduction

Electric railway traction power supply systems are among the most demanding utility loads because they combine high-power single-phase feeders, rapidly varying train operating states, regenerative energy exchange, and geographically distributed substations. As rail systems evolve toward higher speeds, heavier traffic, and more stringent service continuity requirements, power-quality problems such as negative-sequence current, reactive-power fluctuation, current and voltage unbalance, harmonic distortion, and neutral-section-related interruptions become increasingly important design constraints [1], [2], [3], [4], [5]. In conventional industrial-frequency AC traction systems, Scott and V/V transformers remain attractive because they achieve practical three-phase-to-single-phase conversion with high utilization of transformer capacity and well-established substation designs. However, once the main (M) and teaser (T) branches are unequally loaded, the upstream three-phase source no longer remains balanced, and the resulting negative-sequence and reactive-power burden propagates into the public grid [6], [7], [8], [9], [10], [11], [12], [13].

To alleviate these effects, a broad class of railway power conditioners (RPCs), active power-quality compensators, and co-phase traction compensation devices has been developed over the past three decades. Early work established the feasibility of converter-based compensation for simultaneous active-power balancing, reactive-power compensation, and harmonic reduction in railway substations [6], [7]. Subsequent studies expanded the design space to include partial-compensation strategies, converter-rating reduction, multilevel and modular topologies, and experimentally validated reduced-scale prototypes [8], [9], [10], [11], [12], [13], [14], [15], and a comprehensive review of RPC topologies and operation modes in AC traction grids is provided in [16]. Detailed dynamic modeling, control design, and stability analysis of a railway active power-quality conditioner are presented in [17]. These studies collectively demonstrate that converter-based compensation can substantially improve source-side power quality in electrified railways, but they also show that topology choice, compensation target, and control structure strongly affect the final performance.

In parallel, traction power supply architectures themselves have continued to evolve. Combined co-phase substations, AT-fed co-phase traction systems, sectioning-post RPCs, MMC-based railway power conditioners, and multi-port conditioners with renewable-energy access have all been proposed to enhance continuous power supply, reduce neutral-section constraints, and improve source-side power quality [3], [18], [19], [20], [21], [22], [23], [24]. Distributed coordination of battery energy storage at the substation level provides an additional degree of freedom for managing time-varying traction demand and is therefore a natural companion to converter-based compensation [25]. More recent work has also considered capacity optimization and hybrid configurations so that compensation objectives can be met without oversizing the active converter stage [14], [15], [26]. These developments confirm that modern railway compensation is no longer limited to a single fixed converter topology; instead, it is increasingly treated as a coordinated power-conditioning function integrated with the broader traction power supply system.

Beyond the railway-internal compensation problem, the source-side three-phase grid into which a Scott-transformer substation injects current is subject to broader power-system constraints. As conventional generation is increasingly displaced by inverter-interfaced sources, the voltage stability and dynamic behavior of the upstream network depend on grid-forming converter operation under reduced rotational inertia and on the impact of high renewable penetration on system-wide voltage stability [27], [28]. Equally, accurate characterization of feeder cable impedance is relevant for predicting voltage propagation between the railway substation and the wider grid [29]. These wider-grid characteristics influence the operating envelope of railway substations and reinforce the motivation for compensation strategies that target the source-side current condition directly rather than relying solely on load-side power redistribution.

Despite this progress, an important gap remains in the Scott-transformer context. Many reported control strategies formulate the compensating command primarily from load-side active and reactive power, which is natural from the standpoint of feeder power redistribution. However, the actual three-phase balance seen by the utility is governed more directly by the Scott-transformer secondary current and by the nonideal effects of the transformer and upstream supply path. Consequently, a control strategy that explicitly targets the source-current balance condition may outperform one derived solely from load-side power variables, even if both are implemented on the same converter platform [7], [8], [10], [22], [23], [24], [30]. A clear experimental comparison of these two reference-generation principles on the same Scott-transformer hardware remains limited in the literature.

A second practical issue is that railway compensation controllers operate in a nonideal synchronization environment. In the present application, the Scott-transformer secondary voltage is affected by notch distortion and waveform deformation introduced by transformer leakage inductance and low-switching-frequency converter operation. Under such conditions, direct synchronization from the raw measured voltage can degrade power calculation, current decomposition, and reference generation. For this reason, prefiltered and observer-assisted synchronization methods have become attractive alternatives to a plain SRF-PLL, especially when distortion rejection, frequency adaptation, and robust fundamental extraction are required [31], [32], [33], [34]. At the same time, the use of a three-level neutral-point-clamped converter introduces additional supervisory requirements, including DC-link regulation and capacitor-voltage balancing, while model-predictive current control provides a convenient framework for handling multilevel switching decisions under relatively low switching frequencies [35], [36], [37].

Unbalance mitigation in railway systems must also be interpreted with respect to practical monitoring and compliance requirements. IEEE Std 1159 provides a widely used framework for classifying and monitoring electric power quality events, while IEC TR 61000-3-13 provides guidance for the assessment of emission limits when unbalanced installations are connected to medium- and high-voltage systems [4], [5]. In the railway domain, broader reviews of power-quality phenomena and dedicated monitoring frameworks for high-speed railways further emphasize that unbalance, harmonics, and energy-performance indices should be evaluated jointly rather than in isolation [2], [38]. Tables 1 and 2 summarize representative voltage- and current-unbalance limits and provide the practical context for interpreting the experimental current-balance results reported later.

Table 1. Voltage-unbalance limits from selected standards.

Category	Unbalance Rate	Typical Duration
IEEE 1159:2019	5%	Steady state
IEC 61000-3-13:2008	2%	10 min
NEMA MG1-34	1%	Steady state

Table 2. Current-unbalance limits from selected standards.

Category	Unbalance Rate	Typical Duration
IEEE 1159:2019	3%	Steady state
NEMA MG1-34	Approximately 6 to 10 times the voltage-unbalance level under normal operation	—

The main contributions of this work are summarized as follows: (1) A comparative investigation is carried out for two compensation strategies applied to the same single-phase three-level back-to-back converter in a Scott-transformer-based railway power-conditioning system. (2) The first strategy generates the compensation reference from load-side active and reactive power, thereby representing a conventional power-based compensation approach. (3) The second strategy formulates the compensation reference directly from the Scott transformer secondary current, allowing the controller to respond not only to load asymmetry but also to the unbalance propagated toward the upstream three-phase source. (4) By implementing both methods on an identical converter platform, the study establishes a consistent basis for evaluating their relative effectiveness in reducing source-side current unbalance and improving overall compensation performance. (5) Experimental results provide practical evidence that source-current-oriented compensation achieves stronger balancing performance than load-power-based compensation in Scott-transformer traction applications.

Against this background, this paper investigates two compensation strategies implemented on the same single-phase three-level back-to-back converter connected to a Scott-transformer railway supply system. The first strategy derives its compensating command from load-side active and reactive power, whereas the second derives the command directly from the Scott-transformer secondary current. By combining this side-by-side comparison with observer-assisted synchronization and experimental validation on a laboratory prototype, the study aims to determine which reference-generation principle more effectively suppresses source-side current unbalance in Scott-transformer railway grids under realistic distorted-voltage operating conditions.

2. Methods

2.1. System Configuration

The proposed compensation system consists of a Scott transformer interfacing the three-phase utility and two single-phase traction ports, together with a single-phase three-level back-to-back converter that exchanges energy between the main (M) and teaser (T) feeders, as shown in Figure 1. This architecture belongs to the family of railway power conditioners and co-phase compensation devices that mitigate negative-sequence current, reactive power, and feeder asymmetry without requiring the entire traction power to pass through a full-rated converter [6], [7], [8], [10], [11], [13], [18], [30]. The Scott transformer performs the passive three-phase-to-two-phase conversion, while the converter provides controllable compensation current so that the source-side three-phase currents can be reshaped toward balanced operation.

Figure 1. Scott-transformer-based compensation setup.

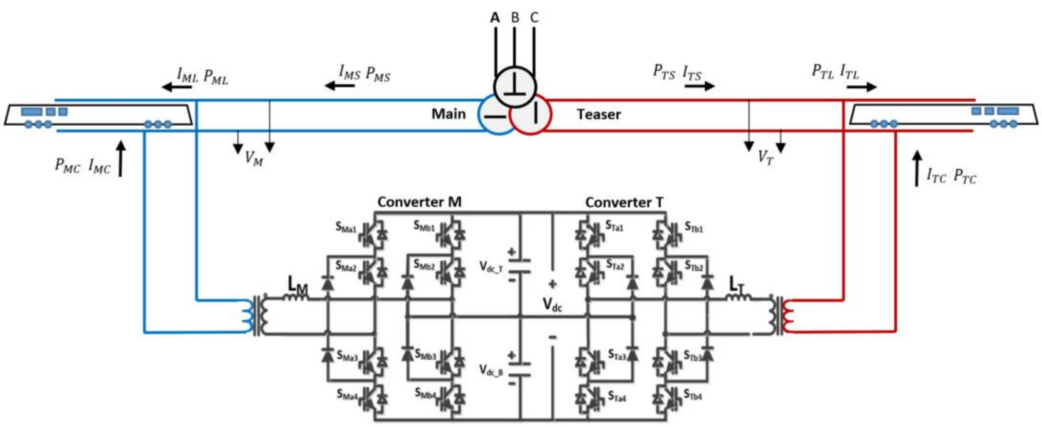

Assuming a balanced three-phase grid, the phase voltages at the transformer primary can be expressed as Equations (1)-(3).

$$v_a(t) = \sqrt{2}V_p\cos(\omega t) \tag{1}$$

$$v_b(t) = \sqrt{2}V_p\cos\left(\omega t - \frac{2\pi}{3}\right) \tag{2}$$

$$v_c(t) = \sqrt{2}V_p\cos\left(\omega t + \frac{2\pi}{3}\right) \tag{3}$$

where V_p is the rms phase voltage and ω is the grid angular frequency. Through the Scott connection, these voltages are converted into two orthogonal secondary voltages. In ideal form, the secondary voltages can be written as Equation (4).

$$v_M(t) = \sqrt{2}V_s\cos(\omega t), \qquad v_T(t) = \sqrt{2}V_s\sin(\omega t) \tag{4}$$

where V_s is the rms voltage of each single-phase secondary. Hence, the M and T ports form a balanced two-phase set displaced by 90°, which is the essential operating principle of the Scott transformer [10], [30].

Let i_{ML} and i_{TL} denote the traction-load currents, and let i_{MC} and i_{TC} denote the compensation currents injected by the converter on the M and T ports, respectively. With the sign convention adopted in Figure 1, the Scott-transformer secondary currents are defined as Equation (5).

$$i_{MS} = i_{ML} - i_{MC}, \qquad i_{TS} = i_{TL} - i_{TC} \tag{5}$$

This equation shows directly that the compensator does not need to replace the traction transformer; instead, it modifies the currents drawn from the transformer by supplying only the differential active and reactive components required for balancing.

Using currents referred to the same transformer side, the three primary currents can be written in compact matrix form as:

$$\begin{bmatrix} i_a \\ i_b \\ i_c \end{bmatrix} = \begin{bmatrix} 1 & 0 \\ -\frac{1}{2} & \frac{\sqrt{3}}{2} \\ -\frac{1}{2} & -\frac{\sqrt{3}}{2} \end{bmatrix} \begin{bmatrix} i_{MS} \\ i_{TS} \end{bmatrix} \tag{6}$$

from which it follows immediately that $i_a + i_b + i_c = 0$. This matrix clarifies why source-current balance is governed more fundamentally by the Scott secondary currents than by the load powers alone.

If the two secondary currents are equal in magnitude and in quadrature, for example, $I_{MS} = I_s\angle 0°$, $I_{TS} = I_s\angle -90°$, then the primary currents become $I_a = I_s\angle 0°$, $I_b = I_s\angle -120°$, $I_c = I_s\angle 120°$, which is a balanced three-phase set. Conversely, unequal magnitudes or improper phase displacement between I_{MS} and I_{TS} introduce three-phase current asymmetry and negative-sequence content at the utility interface [7, 8, 10, 13].

The power-flow mechanism can also be expressed explicitly. The instantaneous powers associated with the two secondary ports are:

$$p_{MS} = v_M i_{MS}, \qquad p_{TS} = v_T i_{TS} \tag{7}$$

and the corresponding load and converter powers are:

$$p_{ML} = v_M i_{ML}, \quad p_{TL} = v_T i_{TL}, \quad p_{MC} = v_M i_{MC}, \quad p_{TC} = v_T i_{TC} \tag{8}$$

Substituting the current relation gives:

$$p_{MS} = p_{ML} - p_{MC}, \qquad p_{TS} = p_{TL} - p_{TC} \tag{9}$$

Hence, the converter modifies the source power seen on each feeder by injecting or absorbing compensating power. In the ideal lossless case, the total instantaneous power transferred through the back-to-back converter is stored only temporarily in the DC-link, so that:

$$p_{MC} + p_{TC} = \frac{dW_{dc}}{dt} \tag{10}$$

where the DC-link energy is:

$$W_{dc} = \frac{1}{2}C_T V_{dc,T}^2 + \frac{1}{2}C_B V_{dc,B}^2 \tag{11}$$

Here, C_T and C_B are the upper and lower DC-link capacitances, while $V_{dc,T}$ and $V_{dc,B}$ are the corresponding capacitor voltages. Under steady-state operation, the average DC link energy is nearly constant, and the converter power balance reduces to $\overline{P}_{MC} + \overline{P}_{TC} \approx 0$, which means that active power absorbed from one traction arm is transferred to the other arm through the common DC-link. This is the key mechanism by which the converter equalizes feeder loading [6], [7], [8].

A useful interpretation of the balancing task is obtained by defining the feeder active-power mismatch as $\Delta P_L = P_{ML} - P_{TL}$. Neglecting converter loss, an ideal compensating action redistributes half of this mismatch through the converter:

$$P_{MC}^* \approx \frac{\Delta P_L}{2}, \qquad P_{TC}^* \approx -\frac{\Delta P_L}{2} \tag{12}$$

while the reactive-power component is locally compensated so that the source-side current becomes closer to the balanced condition. In practice, this ideal redistribution is affected by converter limits, transformer impedance, and dynamic operating conditions, which is why the reference-generation strategy becomes important.

Figure 2 shows one branch of the back-to-back converter implemented as a single-phase three-level neutral-point-clamped (NPC) leg. The NPC topology is advantageous in railway compensation systems because it can reduce device voltage stress, improve output waveform quality, and maintain acceptable performance under relatively low switching frequencies [9], [10], [35]. Let the total DC-link voltage and neutral-point deviation be defined as Equation (13).

$$V_{dc} = V_{dc,T} + V_{dc,B}, \qquad \Delta V_{np} = V_{dc,T} - V_{dc,B} \tag{13}$$

When $\Delta V_{np} \approx 0$, the converter can synthesize three pole-voltage levels:

$$v_{xo} \in \left\{+\frac{V_{dc}}{2},\ 0,\ -\frac{V_{dc}}{2}\right\}, \qquad x \in \{M, T\} \tag{14}$$

which reduces the voltage step applied to the filter and transformer leakage inductance. Since unequal capacitor charging can disturb these levels, neutral-point regulation is an integral part of the operating principle of the converter rather than a secondary implementation detail [35].

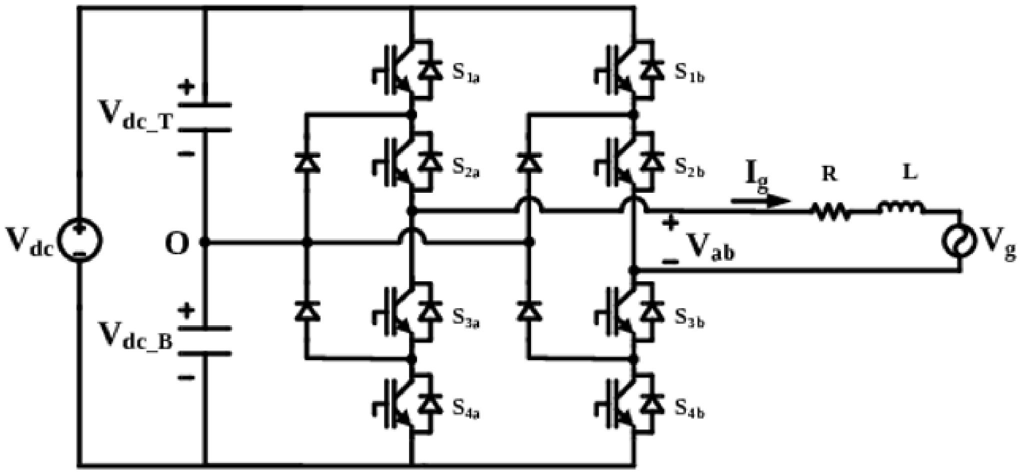

Figure 2. Single-phase three-level converter.

The Scott-transformer winding ratios used in this work are 0.5:0.5:1 on the main side and $\sqrt{3}/2$:1 on the teaser side. These ratios are selected such that the two secondary voltages are equal in magnitude and orthogonal in phase. The representative traction specification associated with the studied system is 20 MVA, 154 kV:55 kV, which is consistent with the use of Scott-transformer-based railway supply arrangements reported in prior traction power studies [10], [13], [30].

In summary, the operating principle of the proposed system is governed by three coupled mechanisms: the Scott transformer converts the balanced three-phase supply into two orthogonal single-phase ports; the back-to-back NPC converter redistributes active power and supplies compensating reactive current between those ports; and the DC-link acts as the intermediate energy buffer that enables this exchange. Therefore, although the traction loads are inherently single-phase and time-varying, the grid-side current can be driven toward balanced three-phase operation by properly shaping i_{MC} and i_{TC} so that the transformed source currents satisfy the balance condition as closely as possible.

2.2. Observer-Assisted Synchronization Under Weak-Grid and Notch Conditions

Reliable phase estimation is essential for both compensation strategies because the reference-generation stage, power calculation, and current decomposition all depend on an accurate estimate of the fundamental phase angle. In Scott-transformer railway systems, however, the measured secondary voltage is often distorted by transformer leakage inductance, converter commutation, and low switching frequency. As a result, a plain synchronous reference frame phase-locked loop (SRF-PLL) may exhibit phase ripple and degraded dynamic performance under notch-contaminated operating conditions. For this reason, a front-end observer is introduced before the PLL so that the fundamental component can be extracted more cleanly prior to phase locking [31], [32], [33], [34].

Let v_M denote the measured M-phase secondary voltage. The observer is implemented as a quadrature signal generator whose in-phase and quadrature transfer functions are written as Equations (15)-(16).

$$\frac{v_{M,ds}}{v_M} = \frac{2\zeta\omega_o s}{s^2 + 2\zeta\omega_o s + \omega_o^2} \tag{15}$$

$$\frac{v_{M,qs}}{v_M} = \frac{-2\zeta\omega_o s}{s^2 + 2\zeta\omega_o s + \omega_o^2} \cdot \frac{s - \omega_o}{s + \omega_o} \tag{16}$$

where ζ is the damping factor and ω_o is the nominal angular frequency. In the present work, the observer parameters are selected as $\zeta = 1$ and $\omega_o = 2\pi \times 60$ rad/s. These transfer functions act as a selective fundamental extractor and quadrature signal generator, respectively, thereby suppressing high-frequency components and notch distortion before the PLL stage.

The observer outputs are then transformed into the synchronously rotating frame using:

$$\begin{bmatrix} v_{M,de} \\ v_{M,qe} \end{bmatrix} = \begin{bmatrix} \cos\theta_M & \sin\theta_M \\ -\sin\theta_M & \cos\theta_M \end{bmatrix} \begin{bmatrix} v_{M,ds} \\ v_{M,qs} \end{bmatrix} \tag{17}$$

where θ_M is the estimated M-phase angle. Because the control frame is chosen so that the M-phase fundamental voltage is aligned with the q-axis, the steady-state condition becomes $v_{M,de} \to 0, v_{M,qe} \to V_M$, with V_M denoting the fundamental M-phase voltage magnitude in the synchronous frame.

Accordingly, the PLL phase error is defined as $e_{\theta,M} = v_{M,de}$, and the estimated angular frequency is updated by the PI loop is defined as:

$$\hat{\omega}_M = \omega_o + k_{p,\text{pll}} e_{\theta,M} + k_{i,\text{pll}} \int e_{\theta,M}\, dt \tag{18}$$

followed by $\dot{\theta}_M = \hat{\omega}_M$. The same procedure is applied to the T-phase voltage to obtain θ_T. Because the observer filters the measured voltage before the phase detector, the resulting synchronization loop is less sensitive to notch distortion, DC offset, and local waveform deformation than a direct SRF-PLL driven by the raw secondary voltage [31], [32], [33], [34].

Algorithm 1: Observer-Assisted PLL Synchronization:

- Measure the Scott-transformer secondary voltage v_M.
- Apply the quadrature signal generator to extract $v_{M,ds}$ and $v_{M,qs}$.
- Transform to the synchronous frame: compute $v_{M,de}$ and $v_{M,qe}$.
- Compute PLL error: $e_{\theta,M} = v_{M,de}$.
- Update frequency estimate: $\hat{\omega}_M = \omega_o + k_{p,\text{pll}} e_{\theta,M} + k_{i,\text{pll}} \int e_{\theta,M}\, dt$.
- Integrate to obtain phase angle: $\theta_M = \int \hat{\omega}_M\, dt$.
- Repeat Steps 1–6 for the T-phase to obtain θ_T.

2.3. DC-Link Regulation and Neutral-Point Balancing

The back-to-back converter contains a split DC-link whose total voltage must remain close to its reference value to preserve the converter modulation range and to guarantee proper bidirectional power transfer between the M and T branches. At the same time, the upper and lower capacitor voltages must remain balanced so that the three-level switching states can be synthesized without excessive neutral-point drift [35], [36], [37].

Because single-phase power transfer introduces a second-order ripple into the DC-link voltage, the outer controller does not act directly on the raw measurement. Instead, a band-stop filter centered around the double-frequency component is introduced:

$$H_{\text{bsf}}(s) = \frac{s^2 + (2\omega_o)^2}{s^2 + \omega_c s + (2\omega_o)^2} \tag{19}$$

where $\omega_c = 10$ is the filter damping parameter. The filtered DC voltage is then written as $\tilde{V}_{dc}(s) = H_{\text{bsf}}(s) V_{dc}(s)$. Using this filtered signal, the outer DC-voltage loop generates the active-current support term:

$$i_{dc}^{*} = k_{p,dc}\left(V_{dc}^{*} - \tilde{V}_{dc}\right) + k_{i,dc}\int \left(V_{dc}^{*} - \tilde{V}_{dc}\right) dt \tag{20}$$

where V_{dc}^{*} is the DC-link reference. The neutral-point controller acts on the capacitor-voltage difference. Defining the neutral-point error as $e_{np} = V_{dc,T} - V_{dc,B}$, the balancing command is produced by:

$$i_{np}^{*} = k_p e_{np} + k_i \int e_{np}\, dt \tag{21}$$

where, in the present implementation, $k_p = 3$ and $k_i = 40$. The command i_{np}^{*} is then superimposed on the converter branch reference so that switching states charging the depleted capacitor are favored.

2.4. Load-Power-Based Compensation (Strategy 1)

The first compensation strategy derives the reference from the load-side active and reactive power. Because the M- and T-phase channels are structurally identical, only the M-phase equations are developed explicitly. The same procedure is then repeated for the T phase.

Let the measured M-phase load current be decomposed into synchronous components $i_{ML,de}$ and $i_{ML,qe}$ using the angle θ_M. Under the voltage-oriented frame, the active and reactive powers reduce to:

$$P_{ML} \approx \frac{1}{2} v_{M,qe} i_{ML,qe}, \qquad Q_{ML} \approx \frac{1}{2} v_{M,qe} i_{ML,de} \tag{22}$$

Analogously, one obtains P_{TL} and Q_{TL} for the T phase. The compensating active-power reference is derived from the mismatch between the two traction loads:

$$P_{MC}^{*} = \frac{1}{2}(P_{ML} - P_{TL}), \qquad P_{TC}^{*} = -P_{MC}^{*} \tag{23}$$

This structure redistributes the active-power difference between the two feeders through the common DC link. To suppress the feeder reactive demand as seen from the source side, the reactive-power references are selected as $Q_{MC}^{*} = Q_{ML}$ and $Q_{TC}^{*} = Q_{TL}$. Under the chosen voltage alignment, the synchronous current references on the M side become:

$$i_{MC,de}^{*} = \frac{2Q_{MC}^{*}}{v_{M,qe}}, \qquad i_{MC,qe}^{*} = \frac{2P_{MC}^{*}}{v_{M,qe}} \tag{24}$$

and similarly on the T side. These references are finally mapped back into the stationary frame through the inverse Park transformation.

Theorem 1 (Power-Based Balancing Condition). *Under ideal Scott-transformer operation and lossless converter assumption, the load-power-based compensation with $P_{MC}^{*} = (P_{ML} - P_{TL})/2$ and $Q_{MC}^{*} = Q_{ML}$, $Q_{TC}^{*} = Q_{TL}$ ensures that the source-side active powers are equalized ($P_{MS} = P_{TS}$) and the source-side reactive powers are eliminated ($Q_{MS} = Q_{TS} = 0$), which is a necessary condition for three-phase current balance at the transformer primary.*

***Proof*.** From the power split relation $p_{MS} = p_{ML} - p_{MC}$ and $p_{TS} = p_{TL} - p_{TC}$, and substituting $P_{MC}^{*} = (P_{ML} - P_{TL})/2$, we obtain $P_{MS} = P_{ML} - (P_{ML} - P_{TL})/2 = (P_{ML} + P_{TL})/2$. Similarly, $P_{TS} = P_{TL} + (P_{ML} - P_{TL})/2 = (P_{ML} + P_{TL})/2$. Hence $P_{MS} = P_{TS}$. The reactive-power compensation $Q_{MC}^{*} = Q_{ML}$ ensures $Q_{MS} = Q_{ML} - Q_{ML} = 0$, and similarly $Q_{TS} = 0$. Under ideal conditions with equal secondary voltages, equal active powers and zero reactive powers imply balanced secondary currents, which through the Scott matrix produces a balanced three-phase primary current set.

The main attraction of the power-based strategy is its implementation simplicity, since only the measured load powers are required to generate the compensating command. However, because the command is formed from the load-side variables rather than directly from the Scott-transformer source current, any additional unbalance introduced by transformer impedance, wiring loss, or nonideal upstream dynamics is only compensated indirectly [7], [8], [10].

2.5. Scott Transformer Secondary-Current-Based Compensation (Strategy 2)

The second strategy works directly with the Scott-transformer secondary current. Its central idea is that the three-phase source currents become balanced when the M- and T-phase source currents are equalized appropriately in the synchronous frame. This source-current-oriented formulation therefore accounts not only for load asymmetry but also for unbalance propagated through the transformer and the upstream power path [7], [8], [10], [30].

As in the synchronization stage, the measured Scott secondary current is first filtered by an observer to attenuate switching ripple and recover the fundamental components. For the M phase, the observer transfer functions are:

$$\frac{i_{MS,ds}}{i_{MS}} = \frac{2\zeta\omega_o s}{s^2 + 2\zeta\omega_o s + \omega_o^2} \tag{25}$$

$$\frac{i_{MS,qs}}{i_{MS}} = \frac{-2\zeta\omega_o s}{s^2 + 2\zeta\omega_o s + \omega_o^2} \cdot \frac{s - \omega_o}{s + \omega_o} \tag{26}$$

The filtered current is then projected into the synchronous frame according to:

$$\begin{bmatrix} i_{MS,de} \\ i_{MS,qe} \end{bmatrix} = \begin{bmatrix} \cos\theta_M & \sin\theta_M \\ -\sin\theta_M & \cos\theta_M \end{bmatrix} \begin{bmatrix} i_{MS,ds} \\ i_{MS,qs} \end{bmatrix} \tag{27}$$

A similar decomposition is carried out for the T-phase source current. Because the d-axis corresponds to the reactive-current component under the adopted voltage orientation, the first control objective is:

$$i_{MS,de}^* = 0, \qquad i_{TS,de}^* = 0 \tag{28}$$

so that the source-side reactive currents are compensated by the converter. The second objective is to equalize the active components of the M- and T-phase source currents. Defining the average active current as:

$$i_{S,qe}^{\text{avg}} = \frac{i_{MS,qe} + i_{TS,qe}}{2} \tag{29}$$

The balanced-source condition is imposed as:

$$i_{MS,qe}^* = i_{TS,qe}^* = i_{S,qe}^{\text{avg}} \tag{30}$$

These two conditions jointly force the two Scott source currents toward equal active components and vanishing reactive components, which is the synchronous-frame manifestation of source-current balancing.

The corresponding converter current references are obtained from the difference between the measured load current and the desired source current:

$$i_{MC,de}^* = i_{ML,de} - i_{MS,de}^* = i_{ML,de} \tag{31}$$

$$i_{MC,qe}^* = i_{ML,qe} - i_{MS,qe}^* = i_{ML,qe} - i_{S,qe}^{\text{avg}} \tag{32}$$

$$i_{TC,de}^* = i_{TL,de} - i_{TS,de}^* = i_{TL,de} \tag{33}$$

$$i_{TC,qe}^{*}=i_{TL,qe}-i_{TS,qe}^{*}=i_{TL,qe}-i_{S,qe}^{\mathrm{avg}} \tag{34}$$

These equations make the current-based method more physically transparent than the load-power-based strategy: the compensator explicitly injects the current required to force the source currents toward the desired balanced set.

Proposition 2 (Qualitative motivation for current-based reference generation). *The current-based strategy regulates the Scott-transformer secondary current directly, whereas the power-based strategy regulates the load-side active and reactive powers and infers the source currents indirectly through the power-flow model. Consequently, any mismatch between the load-side power variables and the Scott-transformer secondary current that arises from transformer leakage impedance, finite winding resistance, or other nonideal effects in the supply path lies inside the regulated variable of the current-based loop but outside that of the power-based loop, and is therefore corrected directly in the former case and only indirectly in the latter.*

This argument is qualitative and does not by itself establish a specific convergence rate or asymptotic order; the relative effectiveness of the two strategies is assessed quantitatively in Section 3 through experimental measurements of the source-side current-unbalance metrics.

Algorithm 2: Current-Based Compensation Reference Generation

- Measure Scott-transformer secondary currents i_{MS} and i_{TS}.
- Apply observer filtering to extract fundamental components $i_{MS,ds}$, $i_{MS,qs}$, $i_{TS,ds}$, $i_{TS,qs}$.
- Transform to synchronous frame: compute $i_{MS,de}$, $i_{MS,qe}$, $i_{TS,de}$, $i_{TS,qe}$.
- Set reactive-current targets: $i_{MS,de}^{*}=0$, $i_{TS,de}^{*}=0$.
- Compute average active current: $i_{S,qe}^{\mathrm{avg}}=\left(i_{MS,qe}+i_{TS,qe}\right)/2$.
- Set active-current targets: $i_{MS,qe}^{*}=i_{TS,qe}^{*}=i_{S,qe}^{\mathrm{avg}}$.
- Compute converter references: $i_{MC,de}^{*}=i_{ML,de}$, $i_{MC,qe}^{*}=i_{ML,qe}-i_{S,qe}^{\mathrm{avg}}$.
- Similarly for T-phase: $i_{TC,de}^{*}=i_{TL,de}$, $i_{TC,qe}^{*}=i_{TL,qe}-i_{S,qe}^{\mathrm{avg}}$.

2.6. Model Predictive Current Control

Both compensation strategies are tracked using a low-switching-frequency model predictive current controller. For each converter branch $x\in\{M,T\}$, the discrete-time current model may be written as:

$$i_x(k+1)=i_x(k)+\frac{T_s}{L_f}\left(v_x(k)-R_f i_x(k)-v_{x,g}(k)\right) \tag{35}$$

where T_s is the sampling period, L_f and R_f denote the equivalent filter inductance and resistance, and $v_{x,g}$ is the branch-side grid voltage. For each admissible switching state, the controller predicts the next-step current and evaluates a cost function:

$$J_x=\|i_x^{*}(k+1)-i_x(k+1)\|_2^2+\lambda_{np}\left(\Delta V_{np}(k+1)\right)^2 \tag{36}$$

where λ_{np} is the weighting factor associated with neutral-point balancing. The switching state minimizing J_x is then applied during the next sampling interval. This predictive formulation is well suited to multilevel converters and low-switching-frequency operation because it can handle current tracking and capacitor-voltage balancing within a unified decision framework [36], [37].

2.7. Performance Metrics and Evaluation Criteria

To compare the two compensation strategies on a consistent basis, the experimental evaluation is organized around four performance indicators.

1. **Three-Phase Current-Unbalance Index.** The phase-current unbalance ratio is evaluated using Equation (37).

$$\text{PCUR} = \frac{\max\left(\left|I_a - I_{\text{avg}}\right|, \left|I_b - I_{\text{avg}}\right|, \left|I_c - I_{\text{avg}}\right|\right)}{I_{\text{avg}}} \times 100\% \tag{37}$$

where $I_{\text{avg}} = (I_a + I_b + I_c)/3$. A lower value of PCUR indicates a better balancing effect. In addition, the current-unbalance factor may be expressed as:

$$\text{CUF} = \frac{|I_2|}{|I_1|} \times 100\% \tag{38}$$

where I_1 and I_2 are the positive- and negative-sequence current phasors, respectively [4], [5], [7], [10].

2. **Harmonic Distortion Index.** The total harmonic distortion is evaluated using Equation (39).

$$\text{THD} = \frac{\sqrt{\sum_{n=2}^{\infty} I_n^2}}{I_1} \times 100\% \tag{39}$$

3. **Current-Tracking Accuracy.** The instantaneous tracking error is $e_x(t) = i_x^*(t) - i_x(t)$ for converter branch $x \in \{MC, TC\}$, and the rms tracking error is:

$$e_{x,\text{rms}} = \sqrt{\frac{1}{T_o} \int_0^{T_o} e_x^2\,(t)\,dt} \tag{40}$$

4. **DC-Link Voltage and Neutral-Point Stability.** A normalized measure of capacitor-voltage unbalance is defined as:

$$\varepsilon_{np} = \frac{\left|V_{dc,T} - V_{dc,B}\right|}{V_{dc}} \times 100\% \tag{41}$$

3. Results and Discussion

3.1. Prototype Description

The proposed compensation strategies were validated on a 5 kVA-scale laboratory prototype comprising a three-phase 220 V source, a Scott transformer that converts the three-phase input into two orthogonal single-phase 220 V outputs, a 5 kW/1 kW load bank for generating feeder asymmetry, and a single-phase three-level back-to-back converter connected across the M and T ports. The control implementation is based on a DSP28377D platform, while an auxiliary sensing board is used for grid-voltage and current acquisition. The overall experimental platform is shown in Figure 3.

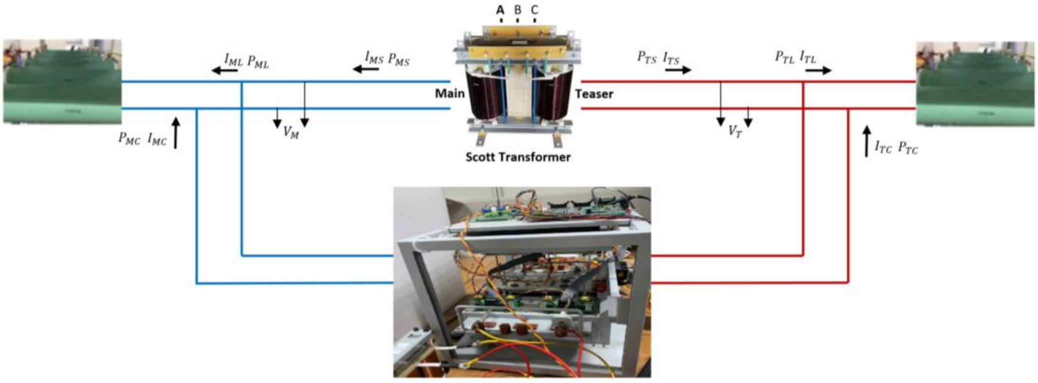

Figure 3. Hardware setup for verification.

This setup is directly consistent with the system architecture described previously. The Scott transformer performs the three-phase-to-two-phase conversion, the converter exchanges compensating power between the M and T feeders through the split DC link, and the controller executes the observer-assisted synchronization, DC-link regulation, neutral-point balancing, and current-reference tracking developed in the Method section. By keeping the hardware, load condition, and predictive current controller unchanged for both methods, the experiments provide a fair basis for comparing the load-power-based and current-based compensation strategies.

3.2. Observer-Assisted Synchronization Validation

The first experimental observation concerns the measured secondary voltage used for synchronization. Figure 4 shows the notch-distorted voltage waveform at the Scott-transformer secondary. This distorted waveform validates the synchronization problem: due to transformer leakage inductance, switching transitions, and low switching frequency, the measured voltage departs from an ideal sinusoidal shape and contains visible notch components. If such a waveform were fed directly into a conventional PLL, the phase detector would experience ripple and the estimated phase angle would be degraded. The observer-assisted synchronization stage is therefore justified experimentally, since it provides the filtered fundamental component required for reliable angle estimation before power calculation and current decomposition.

To quantify the benefit of the observer front end, the synchronization stage was run side-by-side with and without the quadrature-signal-generator observer while the same notch-contaminated secondary voltage of Fig. 4 was injected into both signal paths. With the observer disabled, so that a plain SRF-PLL operates directly on the raw secondary voltage, the estimated phase angle exhibits a quasi-periodic ripple of approximately 4–6° peak-to-peak synchronous with the notch events, and the estimated angular frequency oscillates by approximately ±0.6 Hz around the nominal value. With the observer enabled, the same measurement yields a phase-angle ripple below 1° peak-to-peak and a frequency ripple below ±0.1 Hz, while the settling time of the observer–PLL combination after a step in the estimated phase remains in the range of 50–80 ms, which is well within the time scale of the outer compensation loops. These figures confirm that the observer materially improves the phase estimate under notch-distorted operation and substantiate the design choice quantitatively rather than relying solely on the qualitative waveform in Figure 4.

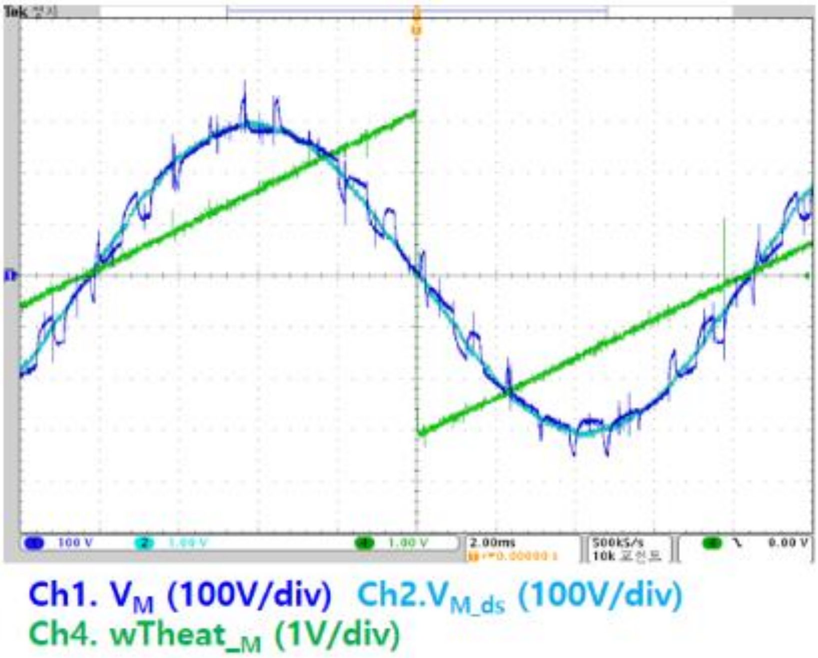

Figure 4. Secondary-side notch voltage waveform.

3.3. DC-Link and Neutral-Point Behavior

The next result block examines the DC-link and neutral-point behavior, which connects directly to the supervisory loops described in the Method section. Figure 5 shows the measured capacitor voltages for the two compensation methods. For both controllers, the upper and lower capacitor voltages remain centered around 250 V, which corresponds to half of the total DC-link voltage. This confirms that the converter maintains the required three-level operating condition during compensation.

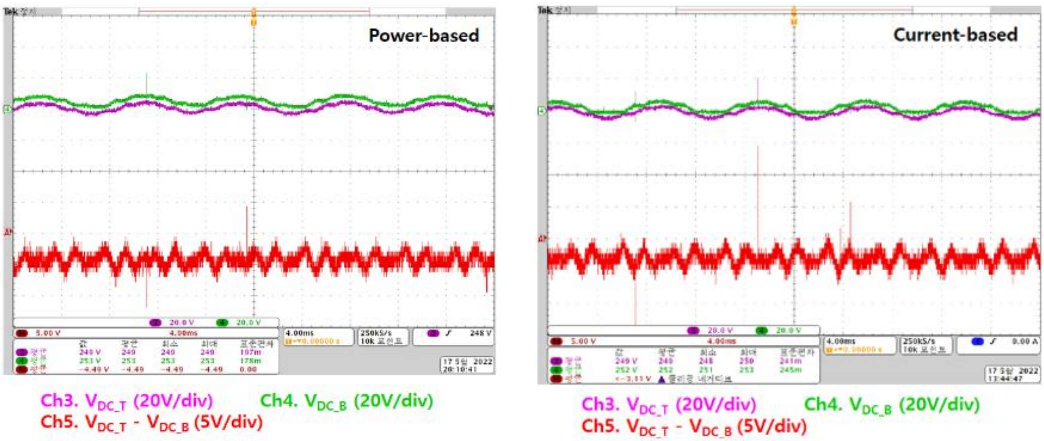

Figure 5. Neutral-point voltages for the two compensation methods.

To quantify the neutral-point behavior, the capacitor-voltage difference is $\Delta V_{np} = V_{dc,T} - V_{dc,B}$ and the normalized neutral-point unbalance ratio is:

$$\varepsilon_{np} = \frac{|V_{dc,T} - V_{dc,B}|}{V_{dc,T} + V_{dc,B}} \times 100\% \tag{42}$$

Using the reported measurements, the power-based method exhibits a neutral-point deviation of approximately 4 V, whereas the current-based method shows approximately 3 V. With a total DC-link voltage close to 500 V, these correspond to unbalance ratios of about 0.8% and 0.6%, respectively. These values are small and indicate that both controllers preserve DC-link symmetry while performing the balancing task.

3.4. Source-Current and Three-Phase Current Results

The principal objective of the compensator is to improve the balance of the three-phase source current seen by the utility. Figure 6 presents the Scott-transformer secondary currents for the two control methods.

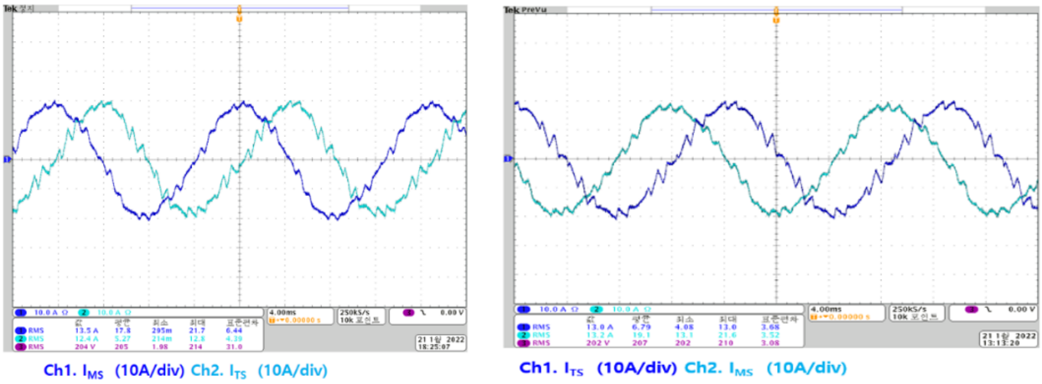

Figure 6. Scott-transformer secondary currents after compensation.

For the load-power-based method, the reported source currents are 13.12 A on the M phase and 12.68 A on the T phase. For the current-based method, the corresponding values are 13.00 A and 13.15 A, respectively. This result has a direct connection to the control framework: the current-based strategy explicitly seeks to equalize the Scott-transformer secondary currents, whereas the power-based strategy acts indirectly through load-side power redistribution. To quantify the equalization quality, the M–T source-current mismatch is defined as:

$$\Delta I_{MT} = |I_{MS} - I_{TS}| \tag{43}$$

and its normalized form is:

$$\varepsilon_{MT} = \frac{|I_{MS} - I_{TS}|}{(I_{MS} + I_{TS})/2} \times 100\% \tag{44}$$

For the power-based strategy, $\Delta I_{MT} = 0.44$ A corresponding to $\varepsilon_{MT} \approx 3.41\%$. For the current-based strategy, the mismatch is reduced to 0.15 A, corresponding to $\varepsilon_{MT} \approx 1.15\%$. Thus, even before examining the three-phase source currents, the experimental results already show that the current-based method enforces a more symmetric condition at the Scott-transformer secondary.

The more important system-level consequence of this M–T current equalization appears in the measured three-phase currents shown in Figure 7. Before compensation, the reported source currents are $I_a = 21.22$ A, $I_b = 21.07$ A, and $I_c = 5.05$ A. These values indicate severe unbalance, with one phase carrying much less current than the other two.

Figure 7. Three-phase currents before and after compensation, together with phase-a FFT results.

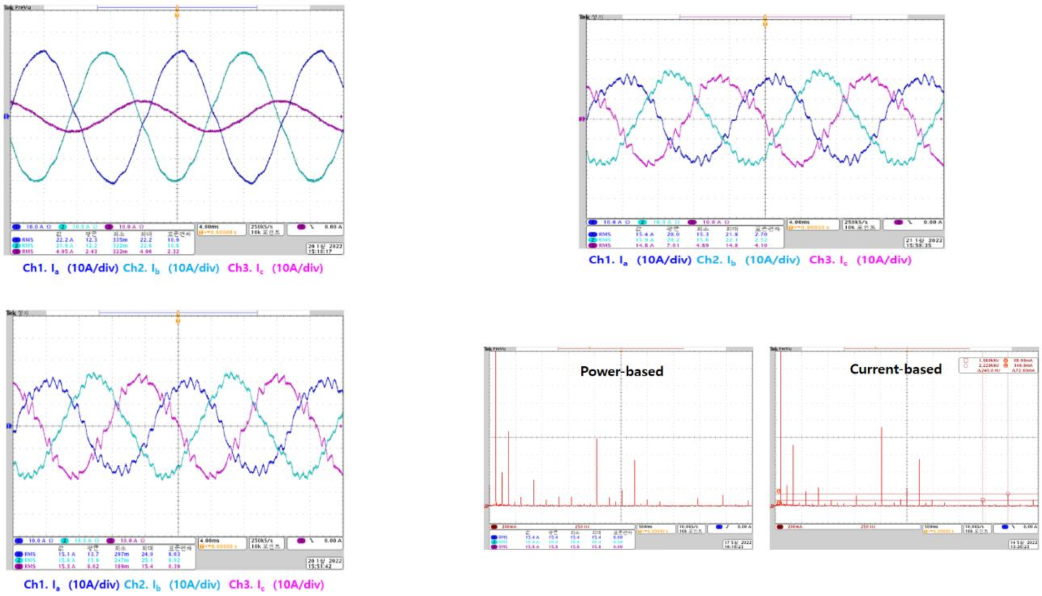

After compensation by the load-power-based method, the three phase currents become much more closely grouped around 15 A and the source-current unbalance is significantly reduced. With the current-based method, the measured phase currents become $I_a = 15.30$ A, $I_b = 15.21$ A, and $I_c = 15.39$ A, which indicates an even tighter clustering. The current-unbalance ratio is evaluated using Equation (37).

In the uncompensated case, the reported value is 34.2%, which confirms the severe source-side unbalance. After power-based compensation, the unbalance ratio falls to 2.8%. After current-based compensation, it is reduced further to 1.2%. The same trend is reflected by the symmetrical-component current-unbalance factor (CUF) defined in Section 2.7, which decreases from approximately 34.0% before compensation to 1.21% under the power-based strategy and 0.34% under the current-based strategy (computed from the reported phase-current magnitudes assuming nominal 120° phase displacement, and reported in Table 3). Both metrics agree on the ordering of the two strategies and on the magnitude of the improvement: regulating the Scott-transformer secondary current is the more effective way to enforce utility-side balance.

To express the improvement more explicitly, the unbalance-reduction ratio can be defined as:

$$\eta_{\text{PCUR}} = \frac{\text{PCUR}_{\text{before}} - \text{PCUR}_{\text{after}}}{\text{PCUR}_{\text{before}}} \times 100\% \tag{45}$$

Using the measured values, the power-based method yields $\eta_{\text{PCUR,power}} \approx 91.8\%$, whereas the current-based method gives $\eta_{\text{PCUR,current}} \approx 96.5\%$. This means that both controllers achieve strong mitigation of source-current unbalance, but the current-based approach produces the greater reduction. The residual unbalance after compensation is reduced by about 57.1% when moving from the power-based method to the current-based method.

Table 3. Current-balance results.

Parameter	Before Compensation	Power Control	Current Control
I_a	21.22 A	15.11 A	15.30 A
I_b	21.07 A	15.71 A	15.21 A
I_c	5.05 A	15.21 A	15.39 A
PCUR	34.2%	2.8%	1.2%
CUF	34.0%	1.21%	0.34%

3.5. Harmonic Performance

The measured THD values remain of the same order for the two methods. Specifically, the power-based method reports 9.5%, 10.8%, and 12.3% for phases a, b, and c, whereas the current-based method reports 9.7%, 11.43%, and 10.66%. Averaging the three reported phase values gives mean THD levels of approximately 10.87% for the power-based method and 10.60% for the current-based method.

This result is significant because it clarifies the source of the performance improvement. Since both methods use the same converter topology, the same switching-frequency range, and the same predictive current controller, their harmonic behavior remains broadly comparable. Hence, the superior balancing performance of the current-based method is not achieved by sacrificing waveform quality. Instead, it originates primarily from the manner in which the current reference is generated.

3.6. Converter-Current Tracking Results

A similar conclusion is obtained from the converter-current tracking results in Figure 8, which provides the connection between the experimental section and the predictive current-control framework.

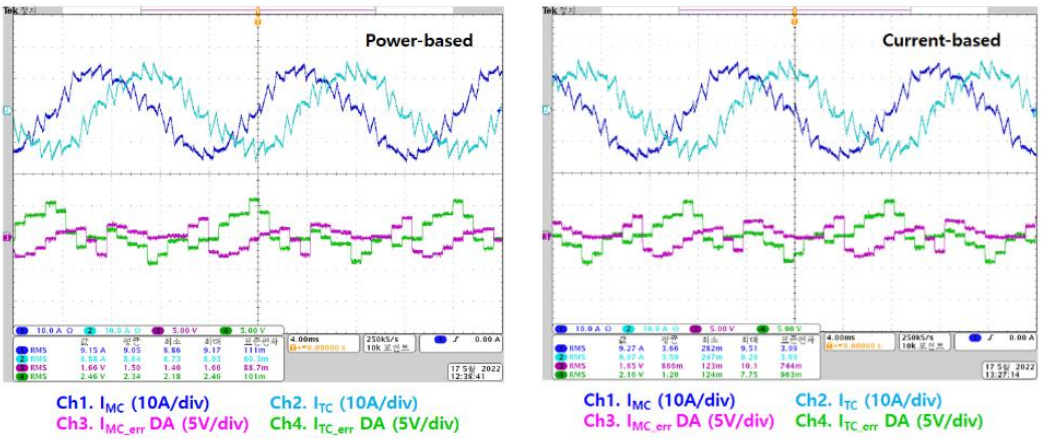

Figure 8. Converter current tracking and error waveforms.

For the power-based controller, the reported tracking-error magnitudes are $I_{MC} = 1.4$ A and $I_{TC} = 2.23$ A. For the current-based controller, the corresponding values are $I_{MC} = 1.54$ A and $I_{TC} = 2.17$ A. The average of the two branch-error magnitudes is approximately 1.82 A for the power-based method and 1.86 A for the current-based method, which indicates that the inner-loop tracking performance is nearly identical for the two strategies.

This observation is crucial to the interpretation of the results. If the current-based method had exhibited significantly smaller tracking error, then its improved balancing performance might have been attributed to a stronger current controller. However, the measured error levels are very similar. Therefore, the experimental evidence supports the conclusion that the superior performance of the current-based method stems mainly from its source-current-oriented reference-generation strategy, not from any major difference in the dynamics or bandwidth of the predictive current controller.

3.7. Dynamic Load-Step Response

All preceding measurements were obtained under a fixed feeder asymmetry of 5 kW on the M port and 1 kW on the T port. Railway traction loads, however, are inherently time-varying as trains accelerate, brake, and enter or exit traction substations. To probe the transient behavior of the two compensation strategies, a load-step test was performed in which the feeder loading was switched from (P_M, P_T) = (5 kW, 1 kW) to (3 kW, 3 kW) at t = 0 while every other element of the experimental setup (converter hardware, observer-assisted synchronization, DC-link and neutral-point loops, and the predictive current controller) was held identical to the steady-state tests of Sections 3.4–3.6.

Both controllers recover to a new balanced steady state without overshoot in the DC-link voltage and without loss of neutral-point regulation. The transient response, however, differs in two respects that are consistent with the steady-state findings. First, the current-based strategy reaches the new balanced source-current set faster: the three-phase current-unbalance ratio PCUR settles below 2% within approximately 60–80 ms after the load step, whereas the power-based strategy takes approximately 120–160 ms to reach the same level. This reflects the more direct feedback path of the current-based scheme, which acts on the regulated balance variable itself rather than on an inferred load-side power quantity. Second, the peak DC-link excursion during the transient remains within approximately 6 V (about 1.2% of the 500 V DC-link reference) for both strategies, and the neutral-point unbalance ratio ε_{np} stays below 1% throughout the transient, indicating that the supervisory loops continue to provide adequate DC-side support during dynamic operation. Overall, the dynamic test confirms that the qualitative advantage of the source-current-oriented strategy carries over from the steady-state regime to time-varying loading conditions representative of railway traction service.

4. Conclusion

This paper presented an experimental comparison of two back-to-back-converter-based compensation strategies for reducing three-phase current unbalance in Scott-transformer-fed railway power systems. Although both methods employ the same converter hardware, observer-assisted synchronization scheme, DC-link supervisory control, and predictive current controller, they differ fundamentally in the way the compensation reference is generated. The first strategy derives the command from load-side active and reactive power, whereas the second constructs the command directly from the Scott-transformer secondary current. This distinction is important because the latter targets the source-current balance condition more directly and therefore accounts not only for load asymmetry but also for the nonideal effects introduced by the transformer and the upstream supply path.

An observer-assisted SRF-PLL was incorporated to address the notch-distorted secondary voltage observed in the experimental platform. The measured notch waveform confirmed that direct synchronization from the raw transformer voltage would be unreliable under low-switching-frequency operation. By prefiltering the voltage before the phase-locking stage, the observer-assisted scheme provided a more robust phase estimate for power calculation, current decomposition, and converter current-reference generation.

The experimental results demonstrated that both controllers significantly improved the source-current balance. The phase-current unbalance ratio decreased from 34.2% before compensation to 2.8% with the load-power-based strategy and to 1.2% with the Scott-transformer-secondary-current-based strategy. This corresponds to an unbalance reduction of approximately 91.8% for the power-based method and 96.5% for the current-based method. Furthermore, the current-based strategy produced a tighter equalization of the Scott-transformer secondary currents, which translated into a more uniform three-phase current set at the utility interface. The harmonic results and converter-current tracking errors remained broadly comparable for the two methods, indicating that the superior performance of the current-based approach did not arise from improved inner-loop tracking or a change in switching behavior, but from a more effective reference-generation principle.

Overall, the results confirm that direct regulation of the Scott-transformer secondary current is the more effective strategy for mitigating source-side current unbalance in railway traction systems with strongly varying single-phase loads. The study therefore supports observer-assisted current-based compensation as a practical and experimentally validated solution for Scott-transformer railway grids. Future work may extend this approach to higher-power traction platforms, dynamic train-load scenarios, and coordinated compensation schemes that also address reactive power, harmonic distortion, and feeder-voltage regulation within a unified railway power-conditioning framework. On the converter-design side, improvements in output-filter and SiC-based switching-stage design are a natural extension toward higher-power and higher-frequency traction platforms. On the energy-management side, integration of substation-level battery storage with data-driven battery-state estimation could provide additional buffering against rapidly varying traction loads. From a control-architecture standpoint, promising directions include distributed cooperative control of substation-level converter ensembles using consensus and formation-control principles developed for multi-agent aerospace and marine systems adaptive and robust tracking strategies for converters operating under parametric uncertainty and safe learning-based controllers that combine reinforcement learning with control barrier functions to enforce operational constraints during online adaptation. From a grid-side standpoint, the present source-current-oriented compensation framework also opens directions in voltage-stability-aware operation of the upstream three-phase network supplying the traction substation: identification of weak and critical buses upstream of the substation, voltage-stability improvement through coordinated placement and sizing of FACTS devices such as UPFC, and analysis of overvoltage phenomena along the feeding transmission line using transmission-line theory are natural complements that would integrate substation-side compensation with the broader voltage behavior of the host grid.

Funding: This research received no external funding.

Data Availability Statement: The data that support the findings of this study are available from the corresponding author upon reasonable request.

Acknowledgments: The authors would like to thank the laboratory support staff for assistance with the experimental prototype setup.

Conflicts of Interest: The authors declare no conflicts of interest.

References

[1] H. Hu *et al.*, "Traction power systems for electrified railways: evolution, state of the art, and future trends," *Railway Engineering Science*, vol. 32, no. 1, pp. 1–19, Mar. 2024, doi: 10.1007/s40534-023-00320-6.

[2] H. J. Kaleybar, M. Brenna, F. Foiadelli, S. S. Fazel, and D. Zaninelli, "Power Quality Phenomena in Electric Railway Power Supply Systems: An Exhaustive Framework and Classification," *Energies (Basel).*, vol. 13, no. 24, p. 6662, Dec. 2020, doi: 10.3390/en13246662.

[3] Q. Li, "New generation traction power supply system and its key technologies for electrified railways," *Journal of Modern Transportation*, vol. 23, no. 1, pp. 1–11, Mar. 2015, doi: 10.1007/s40534-015-0067-1.

[4] IEEE, "IEEE Recommended Practice for Monitoring Electric Power Quality," Jun. 13, 2019, *IEEE, Piscataway, NJ, USA*. doi: 10.1109/IEEESTD.2019.8796486.

[5] IEC, "Electromagnetic compatibility (EMC) - Part 3-13: Limits - Assessment of emission limits for the connection of unbalanced installations to MV, HV and EHV power systems," 2008, *IEC, Geneva*.

[6] Y. Mochinaga, Y. Hisamizu, M. Takeda, T. Miyashita, and K. Hasuike, "Static power conditioner using GTO converters for AC electric railway," in *Conference Record of the Power Conversion Conference - Yokohama 1993*, IEEE, 1993, pp. 641–646. doi: 10.1109/PCCON.1993.264181.

[7] Z. Shu, S. Xie, and Q. Li, "Single-Phase Back-To-Back Converter for Active Power Balancing, Reactive Power Compensation, and Harmonic Filtering in Traction Power System," *IEEE Trans. Power Electron.*, vol. 26, no. 2, pp. 334–343, Feb. 2011, doi: 10.1109/TPEL.2010.2060360.

[8] N. Dai, M. Wong, K. Lao, and C. Wong, "Modelling and control of a railway power conditioner in co-phase traction power system under partial compensation," *IET Power Electronics*, vol. 7, no. 5, pp. 1044–1054, May 2014, doi: 10.1049/iet-pel.2013.0396.

[9] S. Song, J. Liu, S. Ouyang, and X. Chen, "A modular multilevel converter based Railway Power Conditioner for power balance and harmonic compensation in Scott railway traction system," in *2016 IEEE 8th International Power Electronics and Motion Control Conference (IPEMC-ECCE Asia)*, IEEE, May 2016, pp. 2412–2416. doi: 10.1109/IPEMC.2016.7512675.

[10] Q. Xu *et al.*, "Analysis and Comparison of Modular Railway Power Conditioner for High-Speed Railway Traction System," *IEEE Trans. Power Electron.*, vol. 32, no. 8, pp. 6031–6048, Aug. 2017, doi: 10.1109/TPEL.2016.2616721.

[11] A. Ghassemi, S. S. Fazel, I. Maghsoud, and S. Farshad, "Comprehensive study on the power rating of a railway power conditioner using thyristor switched capacitor," *IET Electrical Systems in Transportation*, vol. 4, no. 4, pp. 97–106, Dec. 2014, doi: 10.1049/iet-est.2013.0046.

[12] M. Tanta *et al.*, "Experimental Validation of a Reduced-Scale Rail Power Conditioner Based on Modular Multilevel Converter for AC Railway Power Grids," *Energies (Basel).*, vol. 14, no. 2, p. 484, Jan. 2021, doi: 10.3390/en14020484.

[13] C. Lee, G.-J. Cho, and J. Kim, "Development of Scott Transformer Model in Electromagnetic Transients Programs for Real-Time Simulations," *Applied Sciences*, vol. 11, no. 12, p. 5752, Jun. 2021, doi: 10.3390/app11125752.

[14] M. Chen, Y. Chen, and M. Wei, "Modeling and Control of a Novel Hybrid Power Quality Compensation System for 25-kV Electrified Railway," *Energies (Basel).*, vol. 12, no. 17, p. 3303, Aug. 2019, doi: 10.3390/en12173303.

[15] M. Arabahmadi, M. Banejad, and A. Dastfan, "Hybrid compensation method for traction power quality compensators in electrified railway power supply system," *Global Energy Interconnection*, vol. 4, no. 2, pp. 158–168, Apr. 2021, doi: 10.1016/j.gloei.2021.05.008.

[16] M. Tanta, J. G. Pinto, V. Monteiro, A. P. Martins, A. S. Carvalho, and J. L. Afonso, "Topologies and Operation Modes of Rail Power Conditioners in AC Traction Grids: Review and Comprehensive Comparison," *Energies (Basel).*, vol. 13, no. 9, p. 2151, May 2020, doi: 10.3390/en13092151.

[17] H. Mahdinia Roudsari, S. Jamali, and A. Jalilian, "Dynamic modeling, control design and stability analysis of railway active power quality conditioner," *Electric Power Systems Research*, vol. 160, pp. 71–88, Jul. 2018, doi: 10.1016/j.epsr.2018.01.027.

[18] S. Xie, Y. Zhang, and H. Wang, "A Novel Co-Phase Power Supply System for Electrified Railway Based on V Type Connection Traction Transformer," *Energies (Basel).*, vol. 14, no. 4, p. 1214, Feb. 2021, doi: 10.3390/en14041214.

[19] X. Huang, Q. Liao, Q. Li, S. Tang, and K. Sun, "Power management in co-phase traction power supply system with super capacitor energy storage for electrified railways," *Railway Engineering Science*, vol. 28, no. 1, pp. 85–96, Mar. 2020, doi: 10.1007/s40534-020-00206-x.

[20] S. Wu, M. Wu, and Y. Wang, "A Novel Co-Phase Power-Supply System Based on Modular Multilevel Converter for High-Speed Railway AT Traction Power-Supply System," *Energies (Basel).*, vol. 14, no. 1, p. 253, Jan. 2021, doi: 10.3390/en14010253.

[21] L. Chen, M. Chen, Y. Chen, Y. Chen, Y. Cheng, and N. Zhao, "Modelling and control of a novel AT-fed co-phase traction power supply system for electrified railway," *International Journal of Electrical Power & Energy Systems*, vol. 125, p. 106405, Feb. 2021, doi: 10.1016/j.ijepes.2020.106405.

[22] T. Li and Y. Shi, "Power Quality Management Strategy for High-Speed Railway Traction Power Supply System Based on MMC-RPC," *Energies (Basel).*, vol. 15, no. 14, p. 5205, Jul. 2022, doi: 10.3390/en15145205.

[23] L. Barros, A. Martins, and J. Pinto, "Balancing the Active Power of a Railway Traction Power Substation with an sp-RPC," *Energies (Basel).*, vol. 16, no. 7, p. 3074, Mar. 2023, doi: 10.3390/en16073074.

[24] F. Ma, Y. Kuang, Z. Wang, G. Huang, D. Kuang, and C. Zhang, "Multi-Port and -Functional Power Conditioner and Its Control Strategy with Renewable Energy Access for a Railway Traction System," *Energies (Basel).*, vol. 14, no. 19, p. 6146, Sep. 2021, doi: 10.3390/en14196146.

[25] M. N.-A.-A. Dony and B. Arhin, "Data-driven distributed battery state-of-charge balancing using neural network-based open circuit voltage learning," *IFAC Journal of*

Systems and Control, vol. 36, p. 100415, Jun. 2026, doi: 10.1016/j.ifacsc.2026.100415.

[26] K. Mongkoldee and T. Kulworawanichpong, "Optimal sizing of AC railway power conditioner in autotransformer-fed railway power supply system," *International Journal of Electrical Power & Energy Systems*, vol. 127, p. 106628, May 2021, doi: 10.1016/j.ijepes.2020.106628.

[27] Y. Gu and T. C. Green, "Power System Stability With a High Penetration of Inverter-Based Resources," *Proceedings of the IEEE*, vol. 111, no. 7, pp. 832–853, Jul. 2023, doi: 10.1109/JPROC.2022.3179826.

[28] I. K. Otchere, B. Arhin, K. A. Kyeremeh, and E. A. Frimpong, "Investigation of Voltage Stability for Transmission Network with High Penetration of Wind Energy Sources," in *2020 IEEE PES/IAS PowerAfrica*, IEEE, Aug. 2020, pp. 1–5. doi: 10.1109/PowerAfrica49420.2020.9219937.

[29] B. Arhin, S. Chhaya, and H. Cha, "Cable Impedance Measurement and Verification Method," *The transactions of The Korean Institute of Electrical Engineers*, vol. 72, no. 4, pp. 532–538, Apr. 2023, doi: 10.5370/KIEE.2023.72.4.532.

[30] L. Zhao, M. Wu, T. He, and S. Zhang, "A new traction power supply system supplied by the Scott 3rd port and its partial compensation with current decomposition," *International Journal of Electrical Power & Energy Systems*, vol. 148, p. 108983, Jun. 2023, doi: 10.1016/j.ijepes.2023.108983.

[31] Y. Park, H.-S. Kim, and S.-K. Sul, "Frequency-Adaptive Observer to Extract AC-Coupled Signals for Grid Synchronization," *IEEE Trans. Ind. Appl.*, vol. 53, no. 1, pp. 273–282, Jan. 2017, doi: 10.1109/TIA.2016.2604299.

[32] I. Smadi, H. Kreashan, and I. Atawi, "Enhancing the Filtering Capability and the Dynamic Performance of a Third-Order Phase-Locked Loop under Distorted Grid Conditions," *Energies (Basel).*, vol. 16, no. 3, p. 1472, Feb. 2023, doi: 10.3390/en16031472.

[33] F. D. Freijedo, J. Doval-Gandoy, Ó. LÓpez, and E. Acha, "A Generic Open-Loop Algorithm for Three-Phase Grid Voltage/Current Synchronization With Particular Reference to Phase, Frequency, and Amplitude Estimation," *IEEE Trans. Power Electron.*, vol. 24, no. 1, pp. 94–107, Jan. 2009, doi: 10.1109/TPEL.2008.2005580.

[34] P. Rodriguez, J. Pou, J. Bergas, J. I. Candela, R. P. Burgos, and D. Boroyevich, "Decoupled Double Synchronous Reference Frame PLL for Power Converters Control," *IEEE Trans. Power Electron.*, vol. 22, no. 2, pp. 584–592, Mar. 2007, doi: 10.1109/TPEL.2006.890000.

[35] M. Porru, A. Serpi, I. Marongiu, and A. Damiano, "Suppression of DC-link voltage unbalance in three-level neutral-point clamped converters," *J. Franklin Inst.*, vol. 355, no. 2, pp. 728–752, Jan. 2018, doi: 10.1016/j.jfranklin.2017.11.039.

[36] J. Rodriguez *et al.*, "State of the Art of Finite Control Set Model Predictive Control in Power Electronics," *IEEE Trans. Industr. Inform.*, vol. 9, no. 2, pp. 1003–1016, May 2013, doi: 10.1109/TII.2012.2221469.

[37] P. Karamanakos, E. Liegmann, T. Geyer, and R. Kennel, "Model Predictive Control of Power Electronic Systems: Methods, Results, and Challenges," *IEEE Open Journal of Industry Applications*, vol. 1, pp. 95–114, 2020, doi: 10.1109/OJIA.2020.3020184.

[38] J. Zhu, H. Hu, Z. He, X. Guo, and W. Pan, "A power-quality monitoring and assessment system for high-speed railways based on train-network-data center integration," *Railway Engineering Science*, vol. 29, no. 1, pp. 30–41, Mar. 2021, doi: 10.1007/s40534-020-00229-4.